CO₂ to dimethylcarbonate synthesis: Surface defects and oxygen vacancies engineering on MOF-derived $Ce_xZr_{1-x}O_{2-y}$ catalysts

Sergio Rojas-Buzo [*,1], Davide Salusso [1,2], Andrea Jouve, Edoardo Bracciotti, Matteo Signorile, Silvia Bordiga [*]

Department of Chemistry and NIS Centre, University of Turin, Via Giuria 7, 10125 Turin, Italy

ABSTRACT

Direct reaction of carbon dioxide and methanol to produce dimethylcarbonate (DMC) is an interesting process that allows the synthesis of such valuable product in a more environmentally friendly route than the present technology that is expensive, unsafe and uses toxic raw materials. Unfortunately, this alternative presents intrinsic limitations as the low yield due to thermodynamic limitation and reaction mechanism remains unclear. Herein, we propose a reproducible synthetic methodology of cerium oxide and Ce/Zr solid solutions by calcination of opportune UiO-66(Ce/Zr) MOFs, employed as sacrificial precursors. The higher defectivity of these nanomaterials, corroborated by IR of adsorbed CO, in comparison with commercially-available ones, as those synthesized by traditional sol-gel methods, plays a pivotal role in the direct synthesis of DMC. Lastly, reaction mechanism was systematically and in-depth investigated by *in situ* AP-NEXAFS and MCR-ALS/LCF augmented IR spectroscopy, unveiling the role of oxygen vacancies towards CH_3OH activation.

1. Introduction

Dimethylcarbonate (DMC) is an organic molecule widely employed as green solvent, fuel additive, electrolyte in ion batteries and as intermediate in the production of industrially-relevant products in medicine, pharmacy, chemistry and other fields [1–3]. Among the different synthetic approaches, the direct reaction of CO_2 and methanol is one of the most appropriate and eco-friendly routes, due to CO_2 valorization, generation of H_2O as the only by-product and avoiding expensive, unsafe and noxious raw materials. However, this alternative presents two main challenges: 1) CO_2 is a very stable molecule, whose activation remains not trivial; and 2) water generated during the reaction limits the DMC productivity by poisoning the catalyst and by pushing the reaction equilibrium toward reagents as accumulates along time[4–6]. Considering the process requirements, heterogeneous catalysis results the most practical approach to convert CO_2 into DMC [7,8]. Despite the low DMC yield obtained employing ZrO_2, CeO_2 and their solid solutions as catalysts, they gained a lot of attention not only due to high selectivity toward DMC (~99%), but also to the synergy between its acid-base and redox properties useful for CO_2 and methanol activation [9–11]. For

example, the influence of surface oxygen vacancies (Ce^{3+}-V_o sites) on cerium oxides and its solid solutions (*i.e.*, Bi [12], Ca [13] and Zr [14] doping), providing basic sites, is expected to have an impact on the activation and conversion of CO_2 [15]. In our previous research, we found that the presence of oxygen vacancies on CeO_2 favoured the CO_2 activation through carbonate formation [16]. Subsequently, in the nearness of an oxygen vacancy, methanol is activated to form methoxide, which could react with the adsorbed CO_2 to give the monomethylcarbonate (MMC) intermediate. Finally, the addition of a methyl group generated during methoxide decomposition on the near acidic sites to MMC should lead to DMC [17,18]. However, an excessive strength of these latter could promote the production of dimethyl ether (DME) as by-product, at the expense of DMC yield [19]. In summary, a compromise between surface sites, including acid-base and redox ones, is necessary to afford an enhanced in the catalytic performance. In this sense, Metal-Organic Frameworks (MOFs) as sacrificial precursors of metal oxides represents an innovative methodology to generate nanomaterials with combined acid-base and redox properties and highly exposed active sites [20–22]. This synthetic route also hinders the particle aggregation that is commonly observed in most of the traditional

* Corresponding authors.
  E-mail addresses: sergio.rojasbuzo@unito.it (S. Rojas-Buzo), silvia.bordiga@unito.it (S. Bordiga).
  [1] S. R.-B. and D. S. contributed equally to this work.
  [2] Current address: European Synchrotron Radiation Facility, CS 40220, 38043 Grenoble.

processes (*i.e.,* hydrothermal [23], sol-gel [24], and precipitation ones [25]) [26]. Cerium oxides obtained from the thermal decomposition of Ce-MOFs have demonstrated low-temperature reducibility and consequently the presence of oxygen vacancies on its surfaces [27,28]. This could result into an improvement on the catalytic performance for diverse transformations [29–31]. However, despite the numerous studies reporting MOF precursor calcination to prepare CeO_2 with different morphologies, surface areas, and oxygen vacancies concentration [32–34], only few examples have generated a solid solution by including a second metal unit. Metal incorporation in the MOF structure could be obtained through: 1) the organic linker [35], 2) bimetallic clusters [36]; and 3) a classic wetness impregnation [37]. Among these, the hybrid metallic cluster on the MOF structure seems the most feasible one due to the proximity of the metal atoms and its preservation during the thermal treatment [38]. With all this in mind, we have synthesized three different oxidic nanomaterials, a cerium oxide and two Ce/Zr solid solutions, by a simple and reproducible thermal decomposition of their corresponding UiO-66(Ce/Zr) precursors [34]. The higher number of defective sites obtained by calcination of these sacrificial precursors, in comparison with that presented on commercial or conventionally-obtained oxides, leads to an improvement on the catalytic performance for the DMC synthesis by the direct reaction between CO_2 and methanol, as abovementioned and corroborated by IR spectroscopy of adsorbed CO. In our previous works, we have reported how i) Ce^{3+}-V_o sites can enhance CO_2 activation improving MMC formation [16] and how ii) multivariate curve resolution alternated least square (MCR-ALS) algorithm can be efficiently used to study the intermediates evolution during the reaction of CO_2 and methanol over ZrO_2 catalyst [39]. Here, spectral components, based on methoxide, carbonate and formate species, were extracted by MCR-ALS analysis of *in situ* IR spectra collected during sole CO_2 and CH_3OH adsorption over the ZrO_2 and CeO_2 catalysts. A Linear Combination Fit of the pure components was then applied to IR spectra obtained during the reaction leading to evaluate the different mechanisms occurring on the catalyst surface. Lastly, a complete evaluation of surface and bulk Ce oxidation state during CH_3OH/CO_2 co-adsorption revealed the role of Ce^{3+}-V_o sites during methanol activation.

2. Materials and methods

2.1. MOF-derived oxides synthesis

The UiO-66(Ce/Zr) precursors were synthesized following the protocol described in literature [40,41]. Terephthalic acid (H_2BDC) and *N,N*-dimethylformamide (DMF) were transferred into a round-bottom flask. Subsequently, formic acid (HCOOH, 100%) and an aqueous solution of $(NH_4)_2Ce(NO_3)_6$ (0.53 M) and $ZrO(NO_3)_2 \bullet H_2O$ (0.53 M) were added. Then, the flask reactors were heated under magnetic stirring for 15 min at 100°C using an oil bath. After the synthesis, the reactors were cooled down to room temperature and the materials were collected by centrifugation. Finally, the resulting MOFs were washed, with DMF and acetone, and dried in an oven at 80°C. The final Ce:Zr molar ratio is obtained by varying the ratio between the starting metallic sources (Table 1).

Afterwhile, the as-synthesized MOF precursors were calcined under aerobic conditions (0.5 mL/min) in a tubular flow reactor at 450°C

during 4 h with a heating ramp of 5°C/min to obtain the corresponding oxidic materials denoted as C100 for the pure CeO_2 and C50Z50 (Ce:Zr≈50:50) and C5Z95 (Ce:Zr≈5:95) for the solid solutions. To corroborate the reproducibility on the catalyst's synthesis, three batches of each MOF precursor have been prepared and calcined on different days using the same procedure described above.

2.2. Reference oxides synthesis

Pure CeO_2 and $Ce_{0.5}Zr_{0.5}O_2$ were purchased from Rhodia and Solvay, respectively. Reference $Ce_{0.05}Zr_{0.95}O_2$ was not commercially available, hence it was prepared following standard sol-gel synthesis. Sample synthesis and characterization are described elsewhere [42]. ZrO_2 used as benchmark for *in situ* IR spectroscopy was prepared by sol-gel synthesis as described elsewhere [43].

2.3. Characterization methods

The Powder X-Ray Diffraction (PXRD) measurements were carried out using the Bragg–Brentano geometry with a PANalytical PW3050/60 X'Pert PRO MPD diffractometer equipped with a Cu anode (Kα = 1.5418 Å, Kβ removed by a Ni filter) and a X'Celerator detector. PXRD pattern analysis was conducted with Fullprof software [44]. Unit cell volume was extracted from peak position refinement using a cubic Fm-3 m space group. For sample containing 5% of Ce, also monoclinic P2₁/c polymorph was considered. Crystallite size was calculated from peak shape refinement using Thompson Cox Hastings function [45]. ICP analyses were carried out in a Varian 715-ES ICP-Optical Emission spectrometer after solid disintegration in H_2SO_4/H_2O_2 aqueous solutions. Isothermal N_2 physisorption measurements at Liquid Nitrogen Temperature (LNT) were performed on a Micromeritics 3Flex. Prior to the measurement, the corresponding oxides were degassed at 400°C during 1 h. Specific surface areas using the Brunauer–Emmett–Teller model were extrapolated. HR-TEM was exploited to obtain morphological, structural and elemental information of the samples. The analyses were carried out by using a TEM Jeol JEM 3010 UHR (300 kV, LaB_6 filament) equipped with X-ray EDS analysis by a Link ISIS 200 detector. The samples, in the form of powders, were deposited on a Cu grid, coated with a porous carbon film. The particle size distributions were calculated by measuring ~200 particles using an image analyzer software (Particule).

Fourier Transform IR spectroscopy in transmission mode was employed to characterize surface properties of the materials by following the adsorption of CO as probe molecule. Absorption/transmission IR spectra were collected using a Bruker Vertex 70 spectrophotometer equipped with a Mercury Cadmium Telluride (MCT) cryodetector in the 4000–600 cm^{-1} range with 2 cm^{-1} resolution. Powders were pressed in self-supporting pellets (~7.5 mg/cm^2) and placed in a quartz IR cell suitable for thermal treatments in controlled atmospheres and for spectra recording at LNT. Prior to the measurement, the samples were activated as follow: 1) the pellet was degassed at 400°C (5°C/min) until the pressure reached 5.10^{-4} mbar; 2) then, O_2 (100 mbar) was dosed into the cell and it was maintained at this temperature for 30 min. The cell was then cooled to 300°C and evacuated until the pressure reached 5.10^{-4} mbar; and 3) finally, H_2 (100 mbar) was dosed and maintained at this temperature during other 30 min. Lastly the cell was cooled down to room temperature (RT). To prevent self-oxidation, the reducing gas mixture was maintained until 150°C, while from 150°C to RT, the cell was evacuated prior to the measurement. Without exposing the sample to air, the cell was then connected to a dedicated gas-line and placed in the IR spectrometer. 15 mbar of CO were then dosed and liquid nitrogen was placed in the cell reservoir, allowing cooling until cryogenic temperature (nominal 100 K, in the manuscript referred as LNT). When temperature stabilization was reached, as inferred by the stabilization of the CO signal, the spectra of CO maximum coverage were measured. CO was then degassed through controlled volume expansion, allowing monitoring the decrease on its partial pressure until complete

Table 1
Amount of the different reagents employed during the synthesis of UiO-66 precursors.

Precursor	DMF (mL)	HCOOH (mL)	H_2BDC (g, mmol)	Ce solution (mL, mmol)	Zr solution (mL, mmol)
UiO-66(C100)	30.0	-	0.89, 5.33	10.0, 5.33	-
UiO-66(C50Z50)	18.0	5.2	0.64, 3.84	4.5, 2.40	1.5, 0.80
UiO-66(C5Z95)	36.0	10.3	1.28, 7.74	1.0, 0.53	11.0, 5.86

evacuation.

Raman spectra were collected at room temperature for the as-prepared samples with a Renishaw inVia micro-Raman spectrometer with Ar^+ laser (Spectra Physics) emitting at 514.5 nm. Reported spectra were the result of the average of 30 spectra collected on different portions of the samples to ensure their spatial homogeneity and with an integration time of 30 s.

In situ IR experiments were conducted with a Bruker Invenio spectrophotometer equipped with an Aabspec #2000A cell. The cell was equipped with 13 mm² KBr windows and it allowed heating the sample up to 450°C under the desired gas stream at atmospheric pressure. Gases were flowed with a homemade set-up reported in Fig. S1. Bottles of pure gases (99.9999%) were connected to Bronkhorst EL-flow mass flow-meters. The gases were connected with a manual four-way valve allowing to select between wet and dry gases. One output of the valve was connected to the IR cell while the second to the waste. Background spectrum was collected after flushing the empty cell for 30 min under N_2. Spectra were recorded with 60 kHz and each one was the result of an average of 32 scans (*ca.* 60 s/scan). The samples were pressed into self-supporting (~7.5 mg/cm²) which were held in a gold envelop.

The measurement protocol (Fig. S2) consisted in two main steps: activation and reaction. During activation, the catalyst was heated up to 400°C (5°C/min) under N_2/O_2 flow and it was kept during 60 min. After this step, the sample was considered in its oxidized form (C100-ox and ZrO_2) and it was cooled down to 150°C under $N_2:O_2$ to be then flushed with pure N_2. Contrarily, the reduced form of the catalysts (C100-red, C50Z50 and C5Z95) was obtained by further treating the samples under pure N_2 at 400°C after the N_2/O_2 treatment, then cooling down to 300°C and exposing them to $N_2:H_2$ mixture for 30 min. The pellet was then flushed with pure N_2 and cooled down to 150°C (reaction temperature). Lastly, pure CH_3OH, CO_2 or CH_3OH+CO_2 streams were dosed through the activated pellets. Pure methanol was delivered by flowing N_2 into a saturator containing it. Contrarily, for the reaction, CO_2 was flowed directly into the saturator. All the spectra here reported were subtracted by the spectrum of the activated catalyst *i.e.*, the catalyst before being exposed to CH_3OH, CO_2 or CH_3OH+CO_2 mixture.

To evaluate surface species evolution, we have extracted the spectral components related to pure species (*i.e.*, carbonates, methoxides, *etc.*) by applying the MCR-ALS protocol using the Matlab Gui to the IR spectra collected during pure CH_3OH and CO_2 adsorption experiments [46]. The analysis was applied to the spectral range 3200–2500/1900–800 cm⁻¹ to enhance determination of species presenting similar $\nu(COO)$ while different $\nu(CH)$ modes (*i.e.*, formates and carbonates). As was reported recently [39], we applied the MCR-ALS protocol to improve spectral determination on all the datasets at the same time *i.e.*, spectra collected during adsorption of CH_3OH (or CO_2) over ZrO_2 and CeO_2 were considered as a unique dataset. Regarding CH_3OH adsorption, 5 spectral components were used to describe 98.7% of the variance while during CO_2 adsorption, 3 spectral components allowed to describe 98.5% of the variance. For sake of comparison, the obtained spectra were normalized to 1. MMC and DMC spectra were obtained with the same approach from DMC desorption over ZrO_2, which was already reported in our previous manuscript [39]. A Linear Combination Fit (LCF) procedure using the obtained spectral components was then employed to evaluate species evolution under reaction conditions (*i.e.*, adsorption of CO_2+CH_3OH feed). We have shown the best and the worst fit selected as the dataset with smaller and larger residual variations (residual variation=experimental data-fit), respectively. Indeed, the results reported in Fig. S3 indicate a good agreement between experimental spectra and the fit also in the *worst fit* case. The intensity of an infrared signal depends on its extinction coefficient (ε) and we did not consider it on each band since there are rarely available in literature. Therefore, the obtained concentration profiles (from MCR-ALS and LCF analysis) have to be considered only to follow the evolution while the relative abundance between two components is not meaningful.

Ambient Pressure Near Edge X-Ray Absorption Fine Structure (AP-

NEXAFS) spectra were collected at APE-HE beamline from Elettra Italian Synchrotron radiation source. Thermal treatments (from RT to 350°C, 1 bar of gas atmosphere) were conducted by placing the catalyst in the powder form in a specially designed reactor cell [47]. Ce M_5-edge spectra were collected with Total Electron Yield (TEY) mode in the 880 to 910 eV range and 0.01 eV energy resolution. A similar protocol to that described for the *in situ* IR measurements (Figs. S1 and S2) was followed. N_2 was replaced by He (99.99999%) and the maximum temperature was limited to 350°C. Spectra were energy aligned to the CeO_2 reference spectrum measured simultaneously to the MOF-derived material. Background was subtracted with a 6th order polynomial. All the spectra were background subtracted and energy aligned with the Thorondor software [48].

2.4. Catalytic activity evaluation

The catalytic tests were carried out in a Teflon-lined stainless autoclave as follow: MeOH (6.40 g, 200 mmol), 1-propanol (35 mg, 0.58 mmol), used as external standard, and 80 mg of catalyst were placed in the reactor. Then, the system was purged several times with CO_2 and pressurized up to 30 bar at RT. The mixture was left to stir during 3 h at 140°C, temperature at which the pressure raised to 52 bar. Finally, the reaction was cooled down to RT and analyzed by gas chromatography. The DMC yield was determined using a gas chromatograph equipped with FID and TCD detectors and was normalized by the S_{BET} of the catalyst (Y_s, mmol$_{DMC}$.m⁻²). The reproducible catalytic performance of the C100, C50Z50 and C5Z95 materials obtained from the calcination of different MOF batches was deduced by the error bars reported in Fig. 8. Recyclability tests were performed as follow: the C100 material was recovered from the reaction crude by centrifugation and washed with methanol. The material was then dried at 100°C for 2 h in an oven prior to the next run. The sample obtained after the third cycle was calcined under aerobic conditions (0.5 mL/min) in a tubular flow reactor at 450°C during 4 h with a heating ramp of 5°C/min.

3. Results and discussion

3.1. Structure and morphology of the materials

UiO-66(Ce/Zr) materials were used as precursors for the synthesis of catalysts. The MOFs calcination was conducted at moderate temperature (450°C) since it was observed to be sufficient to remove all the organic components while the agglomeration of their corresponding oxide nanoparticles can be avoided [34]. The PXRD reflections of the as-obtained materials (Fig. S4a) could be indexed to the (111), (200), (220), (311), (222), (400), (311), and (420) planes of CeO_2 face-centered cubic (*fcc*) phase (JCPDS file number 34-394). Peak position refinement highlighted a decrease of unit cell volume in Zr-doped oxides (C50Z50 and C5Z95) in line with its smaller cationic radius respect to Ce^{4+} one, suggesting the formation of solid solutions (Table 2)

Table 2

Physicochemical properties of the MOF-derived materials: N_2 adsorption isotherm report. Chemical composition [a] EDX results. [b] ICP results. [c]Average crystal size from TEM (values in brackets from PXRD analysis). [d]Unit cell volume from PXRD analysis.

Sample	BET surf. area (m²/g)	Chemical composition (Ce:Zr molar ratio)		Average crystal size (nm)[c]	Cubic unit cell volume (Å³)[d]
C100	54.0 ± 1.1	-	-	4.6 ± 1.4 (7)	158.379 ± 0.010
C50Z50	67.6 ± 14.3	40:60[a]	43:57[b]	3.9 ± 0.7 (4)	145.958 ± 0.010
C5Z95	70.3 ± 6.8	4:96[a]	4:96[b]	5.4 ± 1.2 (9)	135.011 ± 0.006

[34,49]. Moreover, the broader and weaker signals detected on the MOF-derived materials in comparison with their corresponding references indicate their smaller crystallite sizes as confirmed from peak shape refinement (Fig. S5, Table S1) [34]. PXRD analysis also indicated as at lower Ce content (<10%), the monoclinic polymorph was observed in both reference and MOF-derived oxides. HR-TEM images reported in Fig. S6 showed as the resulting oxides maintained the octahedral morphology of their MOF precursors [51]. The particle size distribution of the different MOF-derived materials is reported in Fig. S7 and Table 2. C100 is composed of oxide nanoparticles of 4.6 ± 1.4 nm. The 0.311 and 0.269 nm interplanar spacings detected on the HR-TEM images for this material are consistent with (111) and (200) lattice fringes of CeO_2 (Fig. S8), respectively [52]. The average crystal size of C50Z50 is 3.9 ± 0.7 nm. Herein, the detected interplanar spacing was 0.304 nm (Fig. S9), which corresponds with (111) plane. Finally, C5Z95 is based on oxide nanoparticles of 5.4 ± 1.2 nm. Interestingly for this sample we detected (111) planes with interplanar spacings of 0.304 and 0.294 nm (Fig. S9), which agrees with the PXRD patterns reported in d-spacing (Fig. S4b). As a conclusion, C5Z95 material can be considered as the result of Ce-rich ($d_{(111)} = 0.304$ nm) and Ce-poor crystallites ($d_{(111)} = 0.294$ nm) [53]. The chemical composition was assessed by EDX analysis and is fully consistent with the ICP elemental analysis performed on the digested MOF precursors (Table 2). Finally, the surface area of the different oxides was determined by the N_2-adsorption isotherms. All the materials exhibited typical IV isotherm, which is representative of interparticle mesopores obtained during Ce-MOFs calcination (see Fig. S10) [54,55]. BET values obtained for all the samples were always within the intrinsic uncertainty of the technique, apart the case of C50Z50, where a larger fluctuation was observed (see Table 2). Moreover, these values increase with the increasing of the Zr content in the MOF-derived materials, being comparable/slightly lower than those of reference oxides (Fig. S11 and Table S1).

3.2. Unraveling structural defects and oxygen vacancies by IR and Raman spectroscopies

CO chemisorption at LNT followed by IR spectroscopy was employed to probe the nature of the surface sites on the different MOF-derived samples. IR spectra collected during CO desorption on C100 sample (see Fig. 1a) show a band at ~2160 cm^{-1} associated with CO linearly adsorbed on non-defective Ce^{4+} sites on Ce(111) facets [56–58]. On the other hand, a small feature at higher wavenumber (~2176 cm^{-1}) was also detected during the desorption process. This signal could be related to CO interacting with coordinative unsaturated (CUS) Ce^{4+} sites located on Ce(110) planes [57–60]. For comparative purposes, we studied a commercially-available cerium oxide (Rhodia). As can be deduced from Fig. 1d, a component at ~2157 cm^{-1}, associated with the CO-Ce^{4+} adduct, was detected on the reference sample. However, this band is sharper than the one observed on C100 indicating a higher homogeneity of the exposed sites. Moreover, the band at ~2171 cm^{-1}, ascribable to the CO interaction with CUS Ce^{4+} sites, was also detected on the IR spectra [61]. Finally, the CO interaction with hydroxyl groups can be corroborated by the consumption and shifting of their signals after the CO adsorption (see Fig. 1a,d insets). On the other hand, the IR spectra of CO adsorbed on C50Z50 are broader than registered for the pure C100 due to the presence of Ce and Zr centers (Fig. 1b). The ~2167 cm^{-1} component is associated with the interaction of CO with (Ce/Zr)$^{4+}$ sites. Even though this signal is blue-shifted respect to the pure cerium sample, it is difficult to determine whether this is related to Zr^{4+} higher Lewis acidity or CO coverage [62–64]. The asymmetrical character of the spectra, present also in the reference sample (Fig. 1e), suggests the parallel presence of a component at ~2150 cm^{-1}. We assigned this
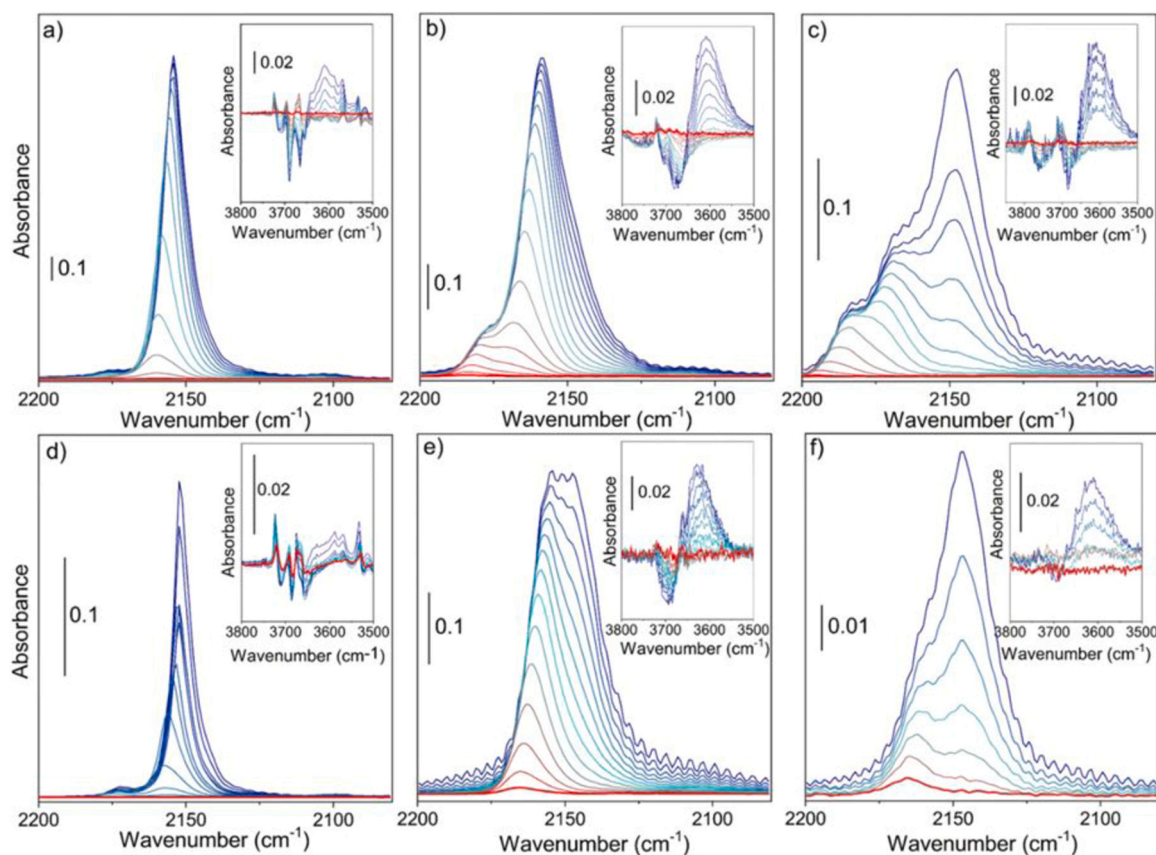

Fig. 1. Difference IR spectra of CO desorption (from blue to red line) at LNT on a) C100, b) C50Z50, c) C5Z95 and their standard references from d) to f), respectively. v(OH) regions are reported in the insets.

signal to CO interacting with OH groups due to: i) the strong relation between the band evolution and the CO partial pressure, ii) its position is blue-shifted with respect to the ν(CO) value of the molecule in gas phase, 2143 cm^{-1} and iii) ν(OH) contribution is red-shifted and consumed with the increase on the CO partial pressure whilst a broad band appears at ~3600 cm^{-1} (see insets Fig. 1b,e) [65]. Moreover, C50Z50 presented a component at higher frequency (~2181 cm^{-1}) with high stability during cell evacuation which is associated with undercoordinated (Ce/Zr)$^{4+}$ sites. The absence of this band in the reference material confirmed the higher surface defectivity of the MOF-derived sample (see Fig. 1e).

Lastly, CO was adsorbed on the activated C5Z95 sample. The main component at ~2150 cm^{-1} is also related with CO interacting with OH groups (see Fig. 1c). Moreover, the perturbation of the OH signals during the CO adsorption corroborates the Brønsted acidity of this material (see insets Fig. 1c,f). On the other hand, two more features at ~2167 and ~2185 cm^{-1} were observed in the IR spectra. The first one is mostly associated with CO adsorbed on non-defective Zr^{4+} sites since the low cerium content in this sample. The blue-shift of this signal with respect to the Ce^{4+} is related to the higher Lewis acidity of the Zr^{4+}. Finally, the signal at ~2185 cm^{-1} is associated with the presence of CUS Zr^{4+} sites. Moreover, it is important to remark the higher surface defectivity of this sample with respect to the reference one where the uncoordinated sites were not detected (see Fig. 1f).

While CO adsorption followed by IR spectroscopy was used to evaluate surface acidity and defectivity, Raman spectroscopy was employed to characterize the oxygen vacancies of the catalysts. Raman spectrum of the as-prepared C100 presented an intense band at 462 cm^{-1} associated to the F$_{2g}$ breathing mode of cubic CeO$_2$ (Fig. S12) [66]. Moreover, side features located at 590 cm^{-1} and 260 cm^{-1}, which are attributed to oxygen vacancies formation in the CeO$_2$ lattice, were detected in both, reference and MOF-derived samples [67,68]. The increase in the intensity of these bands with increasing Zr content, from pure CeO$_2$ to Ce$_{0.5}$Zr$_{0.5}$O$_2$, qualitatively indicates its higher V$_o$ concentration related to a lattice distortion [69]. Finally, samples containing a 5% of Zr show the typical Raman spectra of a mixture of tetragonal and monoclinic ZrO$_2$ phases [70].

3.3. In situ AP-NEXAFS spectroscopy to study the Ce oxidation state

CO$_2$ and CH$_3$OH interaction with cerium-based oxides was studied by AP-NEXAFS spectroscopy. Ce M$_5$-edge spectra collected following the protocol described in the experimental section are reported in Figs. 2 and S13. Ce^{3+} species were already present in the as-prepared C5Z95, in line with Ce/Zr ionic radii differences (Fig. 2f) [34]. Its concentration increased in all the samples after H$_2$ treatment (Fig. 2a-c), and consequently the number of oxygen vacancies (V$_o$). Interestingly, we observed a slightly decrease on the Ce^{3+} content during the cooling in H$_2$. This highlights that 1) sample beam damage is negligible since further reduction would be observed; and 2) AP-NEXAFS in TEY mode, being sensitive to the first surface layers, allows to appreciate surface-to-bulk V$_o$ redistribution occurring by lowering the temperature. Indeed, by considering that after the H$_2$ treatment at 350°C the Ce^{4+} reduction and V$_o$ transport reached an equilibrium, the fact that the V$_o$ transport continues during the cooling in H$_2$ explains the observed partial surface re-oxidation [71]. Moreover, this phenomenon is enhanced on the C50Z50 sample (Fig. 2b), in line with the reported easier oxygen transport on CeO$_2$-ZrO$_2$ solid solutions [72].

After exposing C100-red to pure methanol (Fig. S13a), we observed a relative increment of Ce^{3+} concentration induced by methoxide-to-formate decomposition [73,74]. Contrarily, cerium oxidation state did not change significantly after CO$_2$ adsorption (Fig. S13b). Lastly, when the reduced samples were exposed to CH$_3$OH-saturated CO$_2$ atmosphere (Fig. 2d-f), we observed that C100-red oxidation state does not change (Fig. 2d), while C50Z50 and C5Z95 are further reduced (Fig. 2e and f, respectively). This Ce^{3+} increment, enhanced by the higher Zr concentration, is due to easier Ce reducibility when it is constrained in a ZrO$_2$ matrix [72,75].

3.4. Reaction species evolution investigated by in situ IR spectroscopy

To understand the relation between intermediates evolution and Ce^{3+}-V$_o$ sites, we have followed the reaction by *in situ* IR spectroscopy. Even if the DMC kinetics on ZrO$_2$ and CeO$_2$ catalysts have been deeply studied, we have focused our attention in disclosing the role of Ce^{3+} and
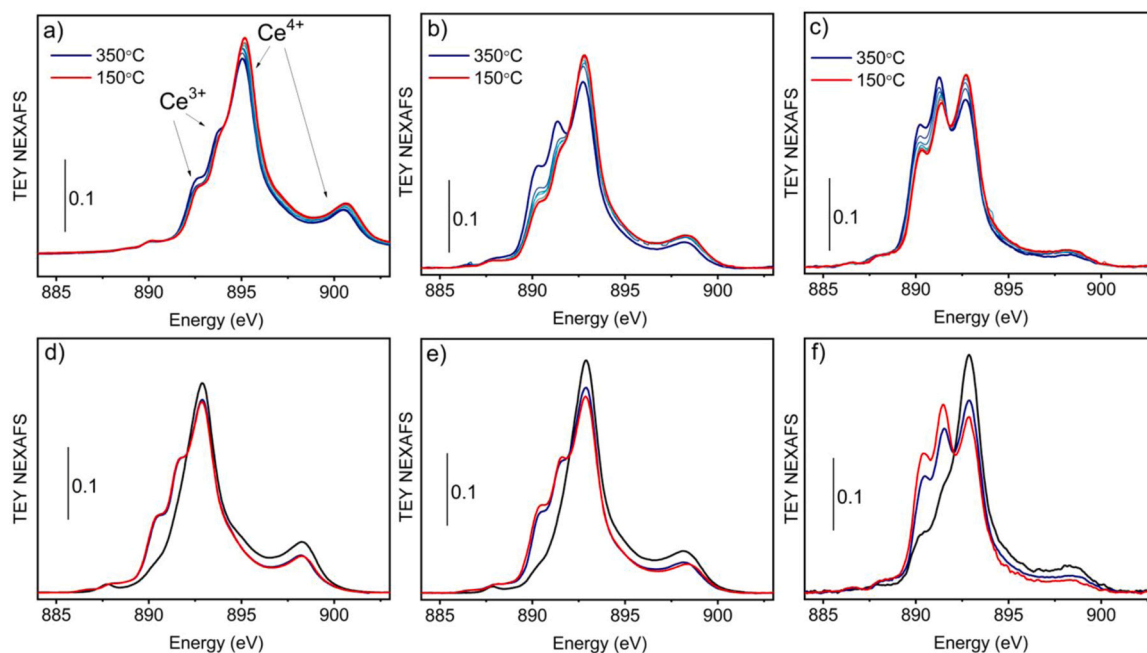

Fig. 2. Ce M$_5$-edge *in situ* AP-NEXAFS spectra measured a-c) during cooling from 350°C to 150°C in H$_2$ over a) C100, b) C50Z50 and c) C5Z95. Temperature decreases from blue to red line. d-f) AP-NEXAFS spectra measured over as-prepared (black line), reduced (blue line) and after exposure to CH$_3$OH-saturated CO$_2$ atmosphere (red line) d) C100, e) C50Z50 and f) C5Z95 catalysts.

defective sites on the MOF-derived samples [13,14,76]. Indeed, species evolution over ZrO_2 was already studied by Bell et al. [77] while we recently reported how those can be extracted by means of MCR-ALS algorithm applied to an *in situ* liquid-phase ATR-IR study [39]. In this work, we first exploited the MCR-ALS protocol to IR spectra collected during sole CH_3OH and CO_2 adsorption, to finally extract separate spectral components of the different isolated species *i.e.*, methoxides, carbonates, *etc.* A Linear Combination Fit of the IR spectra was then employed to evaluate the rate of the different species formed during CO_2+CH_3OH reaction on the catalysts surface.

CH₃OH. To verify that our IR set-up reproduces the results reported in the literature, we have first investigated the CH_3OH adsorption over ZrO_2 at RT [77]. The spectra reported in Fig. S14 showed that gas phase methanol, identified by its characteristic P, Q and R branches, is rapidly accumulated on the catalyst surface. Parallelly, a feature at 1163 cm^{-1} appears, which is ascribed to monodentate methoxide (m-OCH₃) ν(CO) vibration. Tridentate methoxides (t-OCH₃) over ZrO_2, which are usually observed at 1060 cm^{-1}, are likely convoluted with gas phase methanol [77]. On the other hand, we previously reported as methanol adsorption over oxidized and reduced CeO_2 at RT allows to determine the presence of Ce^{3+}-V$_o$ sites through the formation of bidentate methoxide (b'-OCH₃, IR absorption band at 1074 cm^{-1}), which indicates a methoxide bridging to an oxygen vacancy without any chemical interaction with Ce^{3+} [16,62]. Therefore, the same CH_3OH adsorption experiment was carried out at 150°C over ZrO_2 and C100 materials and the results are

summarized in Fig. 3, where four main regions of interest are visible. For sake of clarity, table S2 reports peaks assignment in the full spectral range of interest. As for the adsorption at RT, methanol and methoxide bands can be recognized on zirconia and ceria in the 900–1200 cm^{-1} range. Parallel to methoxide formation, we noticed two intense signals associated to formate ν(HCOO)$_{as/sym}$ vibrations at $\sim$1570 and $\sim$1350 cm^{-1}, respectively, which formation was not observed on ZrO_2 (Fig. S14) and CeO_2 at RT [16]. These bands are shifted to higher frequencies with an increment on the formate bond order. The fact that Ce^{3+} increases the bond order indicates that bidentate formate is mostly formed over Ce^{3+} sites (HCOO-Ce^{3+}) on C100-red [60,78]. Moreover, the first spectrum of methanol adsorbed on C100-red at 150°C presents the Ce^{3+} fingerprint F$^{5/2}$→F$^{7/2}$ transition at 2127 cm^{-1} together with the signal of b'-OCH₃ at 1074 cm^{-1} (Fig. S15). On the other hand, while methanol and Ce^{3+} bands intensity decreases during the adsorption process, formate features begin to be observable (1300–1600 cm^{-1} range). Since, AP-NEXAFS suggested an overall reduction of Ce species during methanol adsorption (Fig. S13), we can hypothesize that the decrease on the Ce^{3+} IR band intensity is related to a variation on the Ce^{3+}-V$_o$ local environment by two possible pathways during the methanol activation over ceria catalyst reported in Scheme 1. In path a), CH_3OH is activated through methoxide formation (Ce-OCH₃), which can be then decomposed to formate (HCOO) causing the cerium reduction (dehydrogenation process) [79]. On C100-red, b'-OCH₃ are the species mostly converted to HCOO, underlying the higher reactivity of
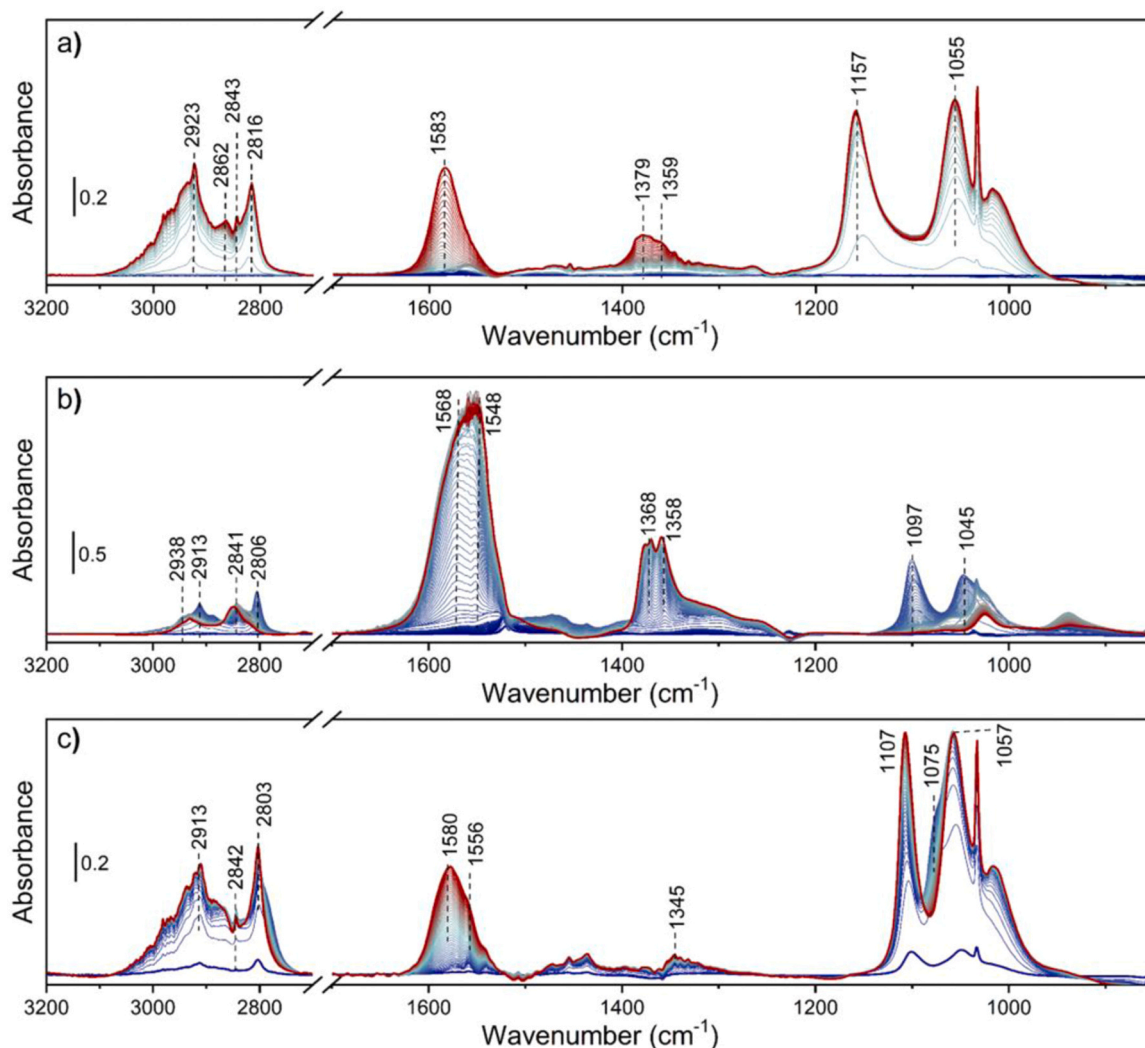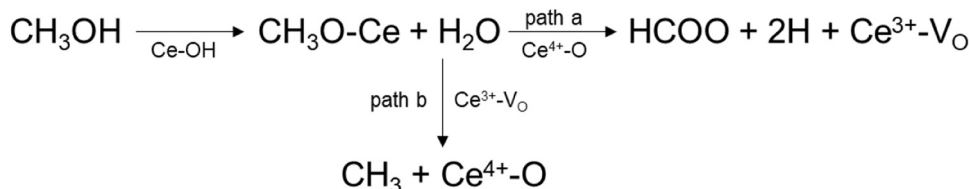

Fig. 3. *In situ* difference IR spectra collected during methanol adsorption at 150°C (from blue to dark red line) over a) ZrO_2, b) C100-ox and c) C100-red.

$$CH_3OH \xrightarrow{\text{Ce-OH}} CH_3O\text{-Ce} + H_2O \xrightarrow[\text{Ce}^{4+}\text{-O}]{\text{path a}} HCOO + 2H + Ce^{3+}\text{-}V_O$$

$$\text{path b} \downarrow Ce^{3+}\text{-}V_O$$

$$CH_3 + Ce^{4+}\text{-O}$$

Scheme 1. Pathways of methanol activation over cerium oxide catalysts.

methoxides bridging to the V_o sites. On the other hand, if methoxides are formed closed to a V_o, the oxygen atom of the methoxide (Ce-OCH$_3$) can partially fill the vacancy (Ce^{3+}-V$_o$) giving a methoxide to methyl decomposition (path b)) [80]. The sensitivity of Ce^{3+} IR band to its chemical environment respect to NEXAFS will be further confirmed by CO$_2$ adsorption experiments described hereafter.

MCR-ALS protocol was then applied to the four datasets (ZrO$_2$ at RT and ZrO$_2$, C100-ox and C100-red at 150°C), leading to isolate five spectral components and their respective concentration profiles (Fig. 4). From the different components, we could identify gas phase methanol (here compared with NIST reference spectrum reported on the bottom of panel a) for clarity), two methoxide species and two different types of formate (Fig. 4a). By the bands position, we could distinguish the methoxides formed on ZrO$_2$ (*i.e.*, CH$_3$O-Zr) and on CeO$_2$ (*i.e.*, CH$_3$O-Ce). However, the same distinction cannot be done for formate species. Indeed, as already observed on the experimental spectra (Fig. 3), bands located at higher frequencies (~1580 cm^{-1} and ~1378 cm^{-1}) can be associated to both bidentate formates (b-HCOO) formed on Zr^{4+} or Ce^{3+} while those at lower wavenumbers (~1548 cm^{-1} and ~1368 cm^{-1}) are ascribed to b-HCOO generated on Ce^{4+} sites (Table S2). As can be deduced from the concentration profile showed in Fig. S14c, methanol is

first accumulated on the ZrO$_2$ surface and rapidly converted to methoxide, while formate species are not detected. At 150°C, methoxides appear faster than gas phase methanol, in line with an easier molecule activation at higher temperature and lower probability of weak physisorption of bare methanol (Fig. 4b). It is noteworthy that at both temperatures, the CH$_3$O-Ce component is detected with a low concentration. Since these species cannot be empirically formed over ZrO$_2$, its presence has to be considered as an artifact induced by the employed MCR-ALS protocol and we can therefore logically consider these species absent in the dataset. Indeed, we can observe how CH$_3$O-Zr spectrum in Fig. 4a presents an anomalous drop in intensity at ~1109 cm^{-1} position, nearly identical to the one main signal on the CH$_3$O-Ce spectrum. After an induction period, b-HCOO/Zr^{4+} starts to rise due to CH$_3$O-Zr decomposition (Fig. 4b). On C100-ox (Fig. 4c), the induction period on the b-HCOO/Ce^{4+} formation is shorter and presents a higher impact on methoxide concentration. Moreover, after ≈ 15 min, we observed the growth of b-HCOO/Ce^{3+} species, indicating that Ce-OCH$_3$ decomposition to formate partially reduces the CeO$_2$ surface in line with the reduction observed by AP-NEXAFS (see path a in Scheme 1 and Fig. S13a). Lastly, on C100-red (Fig. 4d), methoxide appears first than methanol, due to a faster methanol activation. However, after ≈ 20 min,
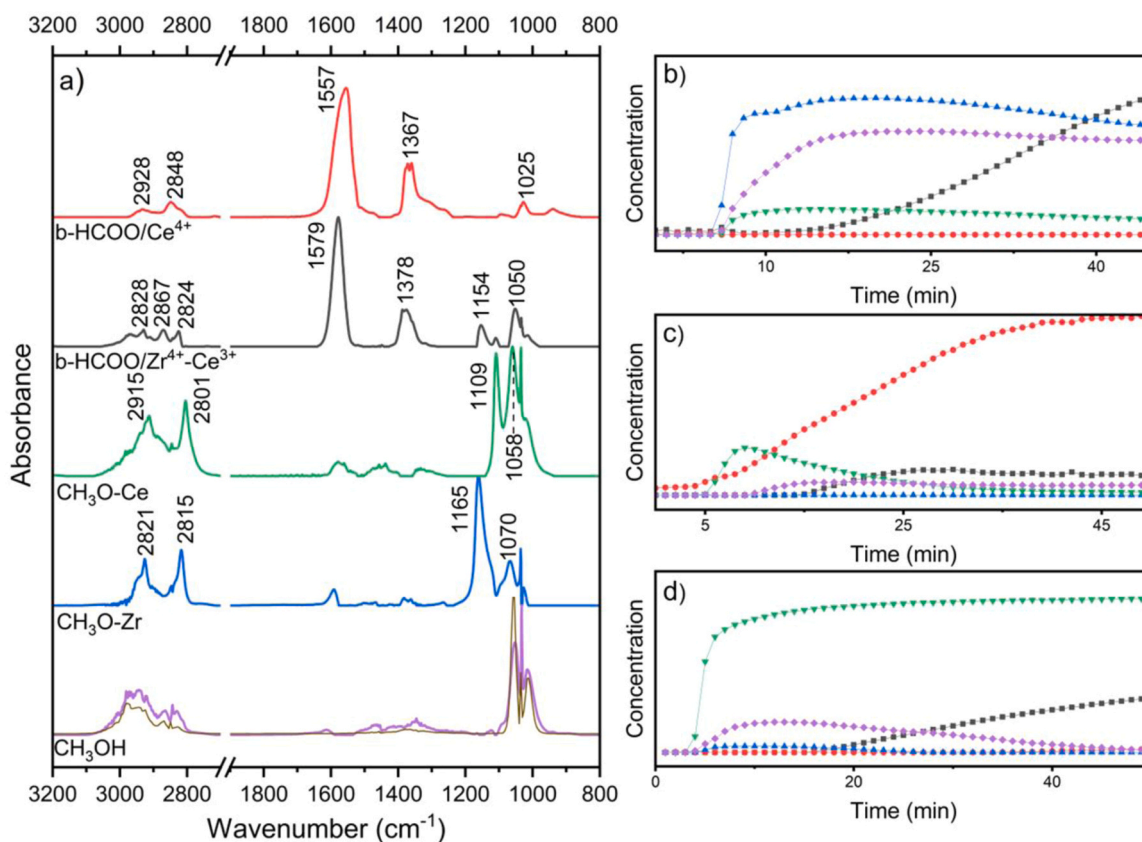

Fig. 4. a) Spectral components and b,c,d) concentration profile extracted by MCR-ALS analysis during CH$_3$OH adsorption/desorption cycles at 150°C over b) ZrO$_2$, c) C100-ox and d) C100-red. CH$_3$OH (purple line and diamonds), CH$_3$O-Zr (blue line and triangles), CH$_3$O-Ce (green line and triangles), b-HCOO/Zr^{4+}-Ce^{3+} (black line and squares) and b-HCOO/Ce^{4+} (red line and circles). Spectrum of gas phase methanol, taken from NIST, is reported on the bottom of panel a) (brown line).

b-HCOO/Ce^{3+} concentration starts to rise while methoxide vibrations remain unchanged. Since the identified methoxide in the MCR-ALS analysis (CH_3O-Ce^{4+}) is not the bridged to the V_o (CH_3O-Ce^{3+}), which was observed to decrease with formate formation from the experimental spectra, we could assume that CH_3O-Ce^{3+} is the one being decomposed to formate.

CO₂. CO_2 adsorption on ZrO_2 is well-known to occur through formation of carbonates and bicarbonates, being the formation rate of the latter faster than the former.[77,81–83] As for CH_3OH, we first monitored the CO_2 adsorption over ZrO_2 at RT. The kinetic evolution and the spectral profile are consistent with those described previously (Fig. 5b). Indeed, under low-temperature conditions, the interaction of CO_2 with the ZrO_2 surface results in the formation of carbonates and bicarbonates, identified from their characteristic $\nu(COO)$ and $\delta(OH)$ vibrations (see assignment in Table S3). The same experiment was then repeated at 150°C to verify the temperature-induced spectral changes (Fig. 5b). While carbonate and bicarbonate species observed at RT can be still identified, the presence of a different type of carbonate, deduced by the appearance of new features at 1547 and 1327 cm^{-1}, indicates that CO_2 activation mechanism changes at higher temperature. On the other hand, a similar spectral shape and convolution is observed on reduced C100 (Fig. 5a), where we can also identify carbonate and bicarbonate species. However, parallely to carbonates growth, the Ce^{3+} band intensity decreases without vanishing completely during CO_2 adsorption, indicating a Ce^{3+}-to-CO_2 charge transfer (see inset in Fig. 5a) [16]. Since NEXAFS spectrum of the C100-red did not change during CO_2 adsorption (see Section 3.3), we can affirm that IR spectroscopy is more sensitive to variations on the local Ce^{3+}-V_o environment. Moreover, by simply comparing the evolution of surface carbonate (CO_3^{2-}) and bicarbonate (h-CO_3^-) with Ce^{3+} band area (Fig. S16a), we can also detect that after an initial increment of both species, the surface carbonates begin to

drop when Ce^{3+}<26% (the Ce^{3+} band extinction coefficient was calculated based on our previous work) [34]. This suggests that the presence of a higher concentration of Frustrated Lewis Pair (FLP) (*i.e.*, high Ce^{3+} content) initially boosts CO_2 activation to carbonates, while when Ce^{3+} content decreases (*i.e.*, lower FLP concentration), CO_3^{2-} formation on Ce^{3+} sites is less favored than on Ce^{4+}-OH, which leads to h-CO_3 generation [16]. It is also evident on the $\nu(OH)$ region (Fig. S16b) that i) bidentate hydroxyl groups (b-OH, 3676 cm^{-1}) are consumed while CO_3 species (3621 cm^{-1}) are generated and ii) monodentate hydroxyl groups (m-OH, 3700 cm^{-1}) are formed in line with their usual observation over oxidized CeO_2 [16].

Finally, the MCR-ALS protocol was applied to isolate spectral components and to describe the species evolution. A first attempt, which considers the three datasets (*i.e.*, CO_2 on ZrO_2 at RT and on ZrO_2/C100-red at 150°C), did not lead to meaningful spectral and concentration components. Indeed, carbonates identification through MCR-ALS routine was already reported to be difficult [39]. For this reason we decided to proceed by analyzing only the spectra collected over ZrO_2, leading to isolate three spectral components that can be ascribed to h-CO_3, monodentate carbonate (m-CO_3^{2-}) and bidentate carbonate (b-CO_3^{2-}) (see Fig. 5c and Table S3 for bands assignment) [77,84–86]. From the concentration profile, we can deduce that carbonate/bicarbonate evolution on the ZrO_2 surface depends on the adsorption temperature. At RT (Fig. 5d), h-CO_3 is preferentially formed during the first minutes of exposure with respect to CO_3^{2-}. With increasing time, bicarbonate species are replaced by carbonates ones. Even if the m-CO_3^{2-} reaches rapidly a steady state, the b-CO_3^{2-} is increasing with a faster kinetic. On the other hand, at high temperature (Fig. 5e), b-CO_3^{2-} is not detected while the concentration evolution of m-CO_3^{2-} and h-CO_3 is similar, being m-$CO_3^{2-}$the only one detected on the first ≈ 15 min. The extracted spectral components were then employed as references for the
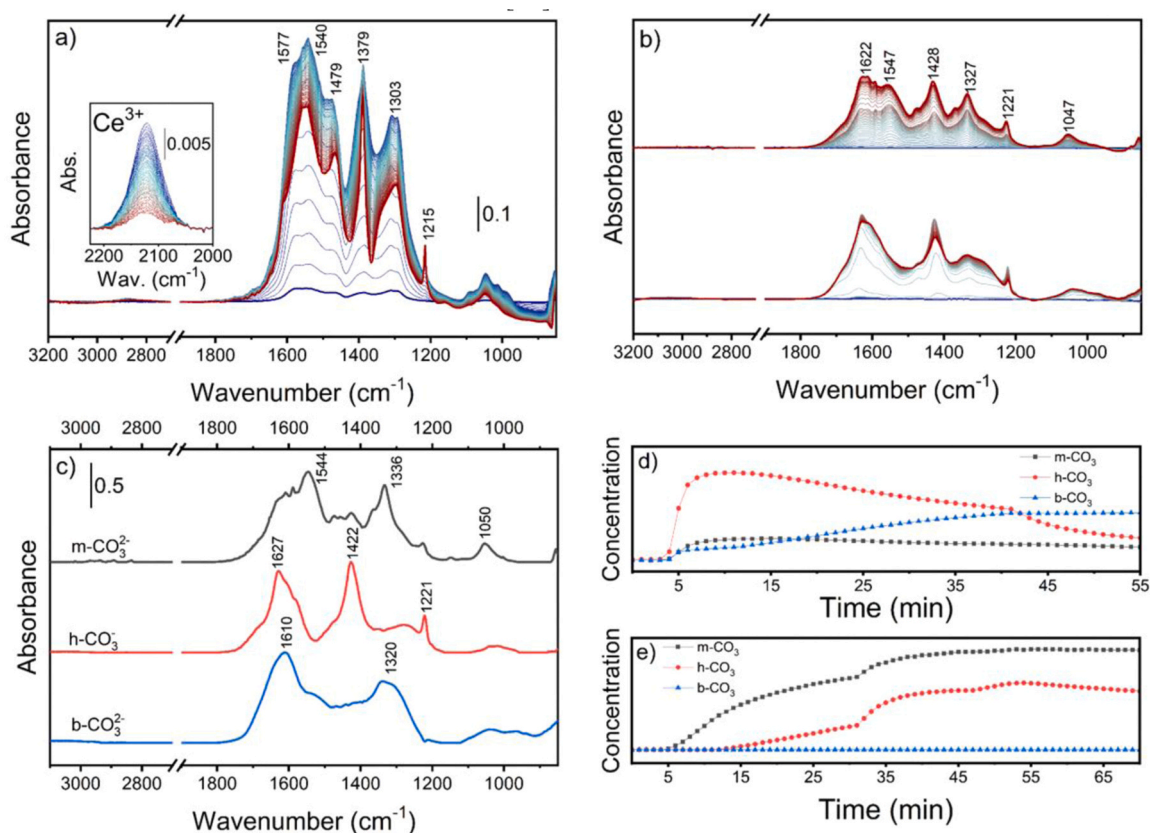

Fig. 5. *In situ* difference IR spectra collected during CO_2 adsorption over a) C100-red at 150°C and b) ZrO_2 at RT (bottom) and at 150°C (top). Adsorption evolves from blue to dark red line. c) Spectral components; d) and e) concentration profiles resulting from the MCR-ALS analysis of ZrO_2 at RT and 150°C, respectively. b-CO_3^{2-} (blue line and triangles), h-CO_3 (red line and circles) and m-CO_3^- (black line and squares).

analysis of the reaction.

CO₂ and MeOH direct reaction. The adsorption of methanol-saturated CO_2 was first monitored over ZrO_2 at RT and 150°C for sake of comparison with previous studies and to evaluate the temperature-induced spectral changes (Figs. S17 and S18, respectively) [77]. At RT, we observed that MMC intermediate is formed (identified by the fingerprint bands at 1600, 1470 and 1350 cm^{-1}), while gas phase methanol rises (see Fig. S17a) [77]. Contrarily, methoxide species and carbonates are barely detectable, being the latter convoluted with MMC. Moreover, the presence of features at ~1700 and ~1300 cm^{-1} suggests the formation of DMC [87,88]. At high temperature (see Fig. S18a), methoxide species are initially observed, however, with increasing time, these are replaced by formates. As deduced by the pure methanol adsorption, formates are related to high temperature-induced methoxide decomposition. On the other hand, the species kinetic clearly changes over Ce-based catalysts: 1) over oxidized C100 (Fig. 6a), methoxide species are stabilized while MMC is convoluted with carbonates; 2) over reduced C100 (Fig. 6b) MMC is initially formed and quickly replaced by formates; and 3) over mixture C50Z50 (Fig. 6c) and C5Z95 (Fig. 6d) oxides, MMC is mainly stabilized. On the other hand, it is noteworthy the presence of a band at 2177 cm^{-1} (indicated in Fig. 6 with an heart symbol), which could be related to i) $CO-Ce^{4+}$ interaction, ii) $2\nu(OCH_3)$ overtone and iii) Ce-H species which are supposed to be present in the 1500–2000 cm^{-1} range [89,90]. Since CO was not able to interact with Ce^{4+} even at RT and hydrides are usually located at lower frequencies, we could assign this feature to methoxide overtone. As already discussed during pure molecules adsorption, Ce^{3+} evaluation depends on the considered reaction and the probing radiation. AP-NEXAFS results discussed above indicated bulk Ce reduction highlighting methoxide-to-formate decomposition (Fig. 2 and path a in Scheme 1). However, from the infrared viewpoint, the Ce^{3+} contribution, initially present in the reduced samples, is consumed during the reaction (Fig. 6b-d insets) suggesting that, at the surface level, the $Ce^{3+}-V_o$ sites are involved in methoxide-to-methyl decomposition (path b in Scheme 1).

To determine the kinetic evolution of the different species, a Linear Combination of the 10 spectral components obtained during sole CH_3OH and CO_2 adsorption (Fig. 7a) was used to fit the CO_2+CH_3OH reaction spectra. The concentration profiles reported in Fig. 7 are in line with the qualitative description of the experimental spectra, however, those offer a more detailed view point on the reaction kinetics. Indeed, we clearly noticed how at RT (Fig. S17), $b-CO_3^{2-}$ and $h-CO_3^-$ are the first species detected on ZrO_2 surface (Fig. S17c) while methanol and methoxide appear only after $\approx$ 7 min (Fig. S17d). During methoxide formation, $h-CO_3^-$ is fully converted into $b-CO_3^{2-}$ and $m-CO_3^{2-}$ species. At the same time, MMC reaches a steady state while DMC concentration drops to zero (Fig. S17e). In line with methanol adsorption at RT, formates are not detected at low temperature. At 150°C (Fig. S18b), MMC is firstly generated together with methoxide and $m-CO_3^{2-}$. Methoxides appear faster than gas phase methanol, in line with an easier molecule activation at higher temperature. After $\approx$ 5 min, $m-CO_3^{2-}$ drops to zero while $HCOO-Zr^{4+}$ starts to grow. DMC was not observed, suggesting its lower stability on the catalyst surface at higher temperatures. On the other hand, we observed a similar concentration profile for all the species on C100-ox, that rapidly reached a steady state. This feature suggests that the presence of $HCOO-Ce^{4+}$ has a minor impact on CeO_2 deactivation. Interestingly, $HCOO-Ce^{3+}$ was detected with comparable concentration than $HCOO-Ce^{4+}$, suggesting that partial surface reduction occurs *via* methanol dehydrogenation. Contrarily, on C100-red (Fig. 7), we observed two-time regions with different concentration profiles. 1) Initially (time<10 min), the catalyst surface is rich in $Ce^{3+}-V_o$ sites and consequently presents a higher activity (MMC and DMC concentration).
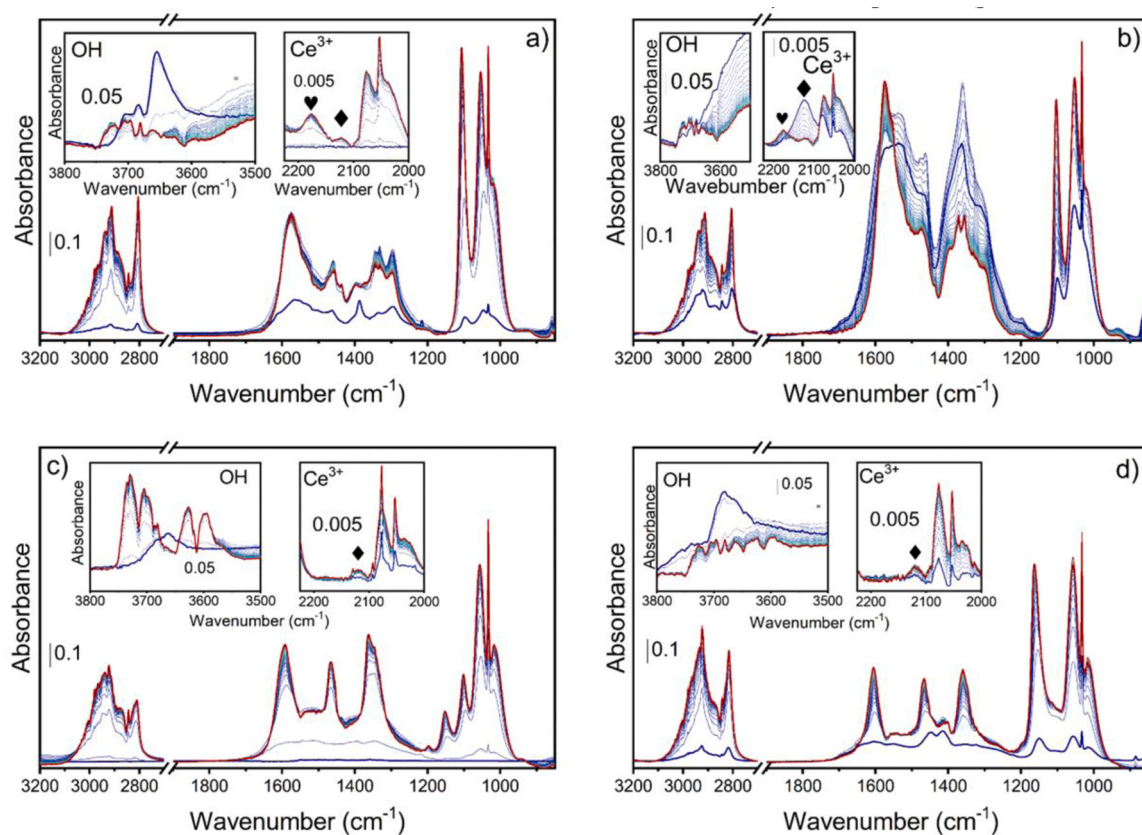

Fig. 6. *In situ* IR spectra collected during CO_2+CH_3OH adsorption at 150°C over a) C100-ox, b) C100-red, c) C50Z50 and d) C5Z95. Gas adsorption goes from blue to dark red line. Details of OH stretching vibrations and Ce^{3+} transitions are reported in the insets. Ce^{3+} and $2\nu(OCH_3)$ overtone are indicated with diamond and heart symbols, respectively.
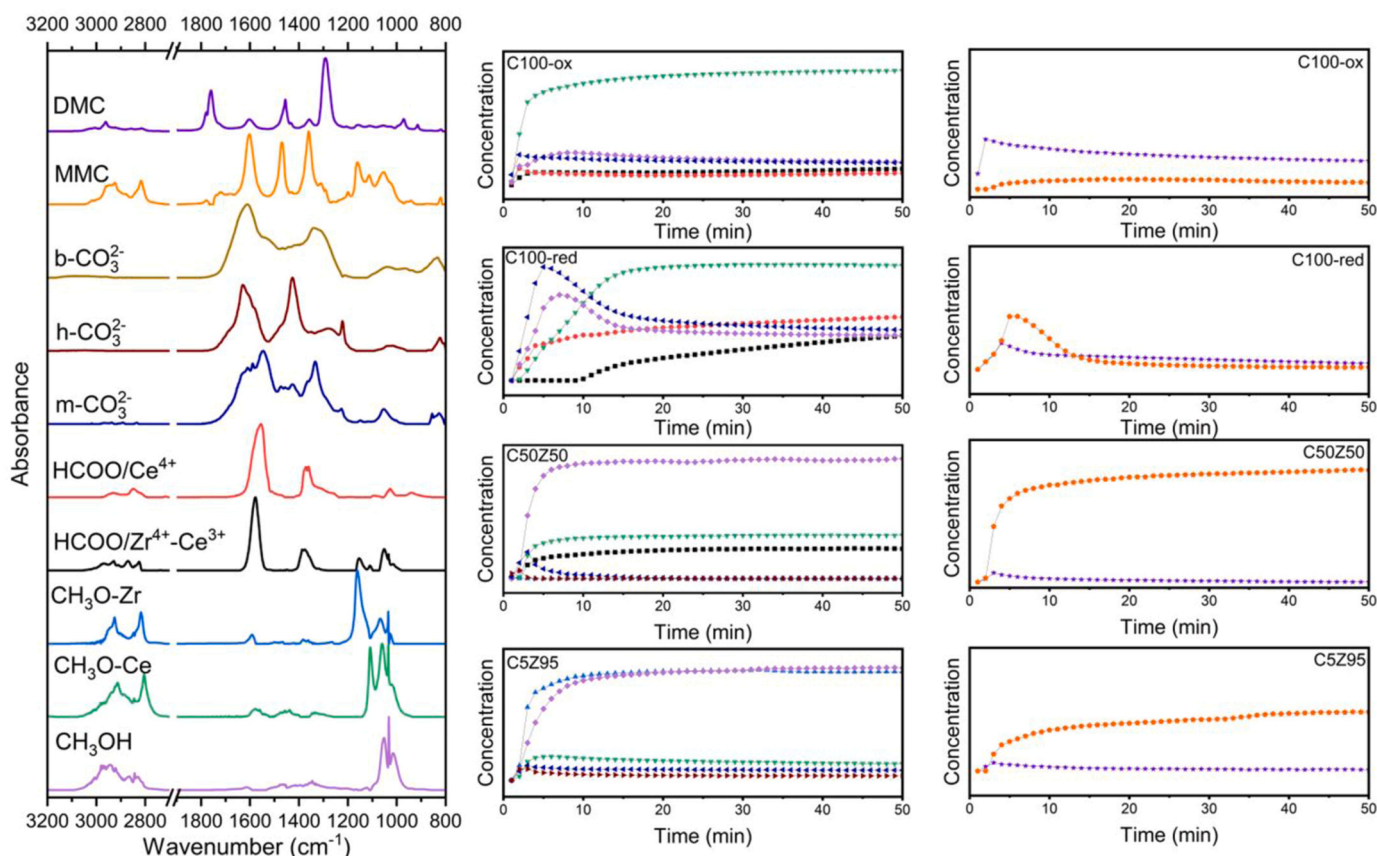
Fig. 7. Main panel: pure spectral components extracted by MCR-ALS analysis of sole CH_3OH and CO_2 adsorption. Minor panels: concentration profiles obtained from LCF of the spectra collected during CO_2+CH_3OH adsorption over C100-ox, C100-red, C50Z50 and C5Z95.

2) After Ce^{3+} saturation, the C100-red deactivates due to a detectable decrease on MMC and DMC concentrations. Parallelly, $HCOO-Ce^{4+}$ component rises while gas phase methanol is consumed, indicating that methanol-to-formate decomposition competes with its reaction with CO_3^{2-} to MMC. The higher formate surface concentration and consequently deactivation detected on C100-red with respect to C100-ox under steady state conditions, could indicate a lower catalytic activity for the DMC synthesis. Finally, on C50Z50 and C5Z95 oxides, MMC is mainly stabilized with respect to HCOO, while $CO_3^{2-}/h-CO_3^-$ species and DMC surface concentrations are negligible.

Finally, Scheme 2 shows the proposed mechanism for the DMC

Scheme 2. Proposed mechanism for the DMC synthesis on C100. Oxygen vacancies are represented by squares.

synthesis using C100 catalyst described in this work. The surface oxygen vacancies promote CO_2 adsorption and activation by carbonate species generation. At a closed Ce-OH site, CH_3OH molecule is activated through methoxy formation (CH_3O-Ce). Activated CO_2 could react with the terminal CH_3O-Ce to produce monomethylcarbonate species (MMC). Subsequent reaction of MMC with methyl group, derived from methoxy decomposition described in the path b of Scheme 1, should lead to DMC.

3.5. Evaluation of the catalytic activity on the DMC synthesis from CO_2 and methanol

Fig. 8 reports the catalytic behavior of the different MOF-derived oxides and their corresponding references on the DMC synthesis from the direct reaction of methanol and CO_2. To account for the influence of the different specific surface area of each sample, the DMC yield was normalized by the BET area of each material. As reported in Fig. 8, the reference samples presented catalytic activities comparable with literature results while the MOF-derived ones displayed higher DMC yields than what usually reported in absence of dehydrating agent (see Table S4) [10,91–94]. Interestingly, the catalytic performance of the C100, C50Z50 and C5Z95 materials prepared from different MOF batches is reproducible since the low standard deviation (see error bars in Fig. 8). The lowest catalytic activity was observed for both samples, MOF-derived and reference, with the lowest Ce content. This fact could be ascribed to the highest Lewis acidity of the Zr^{4+} and consequently the poor catalytic activity observed when ZrO_2 was employed as catalyst on the DMC production (see Fig. 8) [95,96]. The higher amount of coordinative unsaturated Zr^{4+} sites on C5Z95 sample with respect to the reference one, or in other words its higher Lewis acid site concentration, is translated in a poorer catalytic behavior. This remarks the importance of having a compromise of acidic and basic sites. With the increasing of
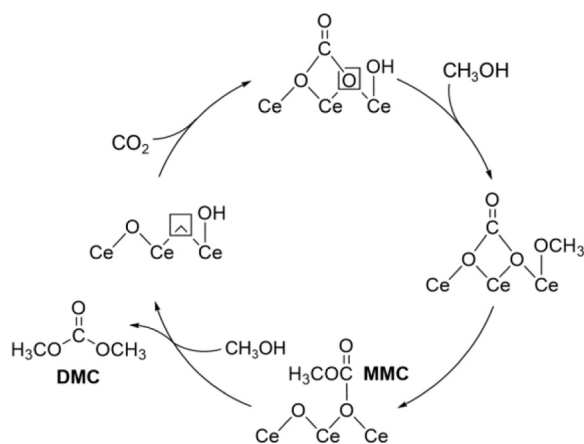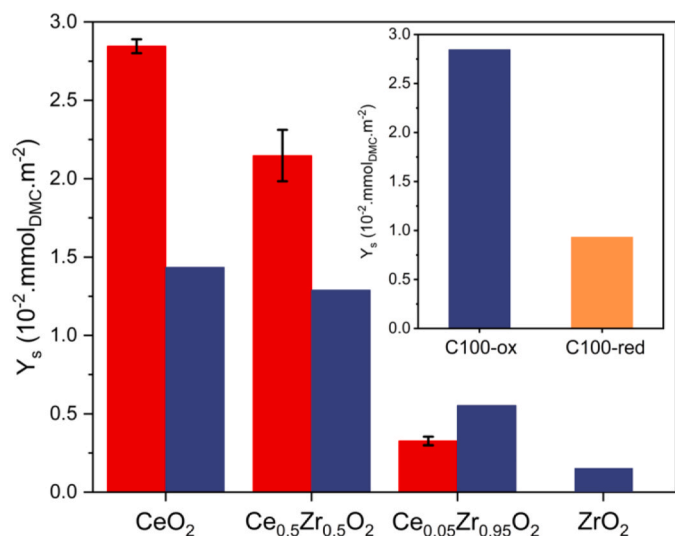
Fig. 8. Normalized DMC yield by S_{BET} area (Y_s) of the different MOF-derived oxides (red bars) and their corresponding references (blue bars). Error bars represent standard deviation (n = 3). Comparative between the catalytic activity of the oxidized and reduced C100 is reported in the inset. (For interpretation of the references to color in this figure legend, the reader is referred to the web version of this article.)

the amount of Ce on the samples, and consequently the concentration of basic sites induced by the presence of V_o, we observe a continuous increment on the catalytic performance. Moreover, the highest defectivity deduced by the CO adsorption experiments on the C50Z50 and C100 MOF-derived materials is translated in a higher catalytic performance for the DMC synthesis. Moreover, this surface defectivity allows Ce^{3+} self-generation during methoxide-to-formate decomposition, which is enough to boost DMC formation with a higher yield than references. On the other hand, we performed a H_2-treatment on the most promising catalyst (C100) to simulate the conditions employed in the *in situ* IR experiment (C100-red). As can be observed in the inset of Fig. 8, C100-red shows a considerably lower catalytic activity in comparison with the oxidized one. The formate saturation on the C100-red surface claimed during the *in situ* IR section, could explain its lower catalytic activity. Finally, we studied the reusability of the C100 in the DMC synthesis. As can be deduced from Figs. S19 and S20a, respectively, the material preserves the catalytic activity and its crystal structure after the first two catalytic cycles. Controversy, the activity decays considerably in the third run. This deactivation could be associated to the adsorption of carbonates and bicarbonates on the catalyst surface deducible by the decrease on the BET area (see Table S5). However, the original catalytic behavior of C100 could be recovered by a simple calcination due to its average crystal size is maintained after the thermal treatment (see Figs. S19 and S20b).

4. Conclusions

In this work, we have synthesized a CeO_2 and two $Ce_xZr_{1-x}O_y$ oxides *via* thermal decomposition of their corresponding UiO-66(Ce/Zr) MOFs, used as sacrificial precursors. CO adsorption monitored by IR spectroscopy confirmed that this synthetic approach allows us to obtain oxides with a higher degree of surface defectivity respect to those prepared by conventional methods. On the other hand, IR spectra collected during adsorption of pure CH_3OH and CO_2 molecules were successfully analyzed by MCR-ALS protocol. The evolution of the extracted spectral components suggested that on both, ZrO_2 and CeO_2 catalysts, methanol is dehydroxylated to methoxide which could be subsequently decomposed to formate/methyl intermediates. Methoxide-to-methyl decomposition is fundamental for MMC methylation; however, this process

causes a Ce^{3+}-V_o sites consumption. This consumption could be countered during the methoxide-to-formate decomposition in which Ce^{3+}-V_o sites are regenerated. LCF analysis of IR spectra collected during CH_3OH+CO_2 reaction on reduced CeO_2 unveiled that an initial high Ce^{3+}-V_o surface concentration enhances CH_3O-Ce dehydrogenation to formate, whose accumulation on the surface causes the catalyst deactivation. If the amount of Ce^{3+}-V_o sites is balanced, the impact on the CeO_2 deactivation is considerably lower. Indeed, despite of that Ce/Zr solid solutions presented an initial higher Ce^{3+} concentration than CeO_2, their overall activities for the DMC synthesis are considerably lower. Lastly, the catalytic performance was found to be 1) reproducible for MOF-derived materials obtained from different MOF batches; and 2) correlated with the concentration of surface defects.

CRediT authorship contribution statement

Bracciotti Edoardo: Investigation, Writing – review & editing. **Jouve Andrea:** Formal analysis, Investigation, Writing – review & editing. **Bordiga Silvia:** Project administration, Resources, Supervision, Writing – review & editing. **Signorile Matteo:** Formal analysis, Investigation, Writing – review & editing. **Salusso Davide:** Data curation, Formal analysis, Investigation, Methodology, Writing – original draft, Writing – review & editing. **Rojas-Buzo Sergio:** Conceptualization, Data curation, Investigation, Supervision, Writing – original draft, Writing – review & editing.

Declaration of Competing Interest

The authors declare the following financial interests/personal relationships which may be considered as potential competing interests: Sergio Rojas-Buzo reports financial support was provided by Polytechnic University of Valencia. If there are other authors, they declare that they have no known competing financial interests or personal relationships that could have appeared to influence the work reported in this paper.

Data availability

Data will be made available on request.

Appendix A. Supporting information

Supplementary data associated with this article can be found in the online version at doi:10.1016/j.apcatb.2024.123723.

References

[1] M.A. Pacheco, C.L. Marshall, Review of dimethyl carbonate (DMC) manufacture and its characteristics as a fuel additive, Energy Fuels 11 (1997) 2–29.
[2] H.-Z. Tan, Z.-Q. Wang, Z.-N. Xu, J. Sun, Y.-P. Xu, Q.-S. Chen, Y. Chen, G.-C. Guo, Review on the synthesis of dimethyl carbonate, Catal. Today 316 (2018) 2–12.

[3] M.A. Rasool, P.P. Pescarmona, I.F.J. Vankelecom, Applicability of organic carbonates as green solvents for membrane preparation, ACS Sustain Chem. Eng. 7 (2019) 13774–13785.

[4] D. Ballivet-Tkatchenko, A. Dibenedetto, Synthesis of linear and cyclic carbonates, in: Carbon Dioxide as Chemical Feedstock, 2010, 169–212. doi: 10.100 2/9783527629916.ch7.

[5] N. Keller, G. Rebmann, V. Keller, Catalysts, mechanisms and industrial processes for the dimethylcarbonate synthesis, J. Mol. Catal. A Chem. 317 (2010) 1–18, https://doi.org/10.1016/j.molcata.2009.10.027.

[6] A. Álvarez, M. Borges, J.J. Corral-Pérez, J.G. Olcina, L. Hu, D. Cornu, R. Huang, D. Stoian, A. Urakawa, CO_2 activation over catalytic surfaces, ChemPhysChem 18 (2017) 3135–3141, https://doi.org/10.1002/cphc.201700782.

[7] J. Ma, N. Sun, X. Zhang, N. Zhao, F. Xiao, W. Wei, Y. Sun, A short review of catalysis for CO_2 conversion, Catal. Today 148 (2009) 221–231.

[8] D. Shi, S. Heyte, M. Capron, S. Paul, Catalytic processes for the direct synthesis of dimethyl carbonate from CO 2 and methanol: a review, Green Chem. 24 (2022) 1067–1089.

[9] K. Tomishige, Y. Furusawa, Y. Ikeda, M. Asadullah, K. Fujimoto, CeO2–ZrO2 solid solution catalyst for selective synthesis of dimethyl carbonate from methanol and carbon dioxide, Catal. Lett. 76 (2001) 71–74.

[10] K. Tomishige, K. Kunimori, Catalytic and direct synthesis of dimethyl carbonate starting from carbon dioxide using CeO2-ZrO2 solid solution heterogeneous catalyst: effect of H2O removal from the reaction system, Appl. Catal. A Gen. 237 (2002) 103–109.

[11] A. Bansode, A. Urakawa, Continuous DMC synthesis from CO_2 and methanol over a CeO2 catalyst in a fixed bed reactor in the presence of a dehydrating agent, ACS Catal. 4 (2014) 3877–3880.

[12] Y. Chen, Y. Li, W. Chen, W.W. Xu, Z. Han, A. Waheed, Z. Ye, G. Li, A. Baiker, Continuous dimethyl carbonate synthesis from CO_2 and methanol over BixCe1−xOδ monoliths: effect of bismuth doping on population of oxygen vacancies, activity, and reaction pathway, Nano Res. 15 (2022) 1366–1374, https://doi.org/10.1007/s12274-021-3669-4.

[13] B. Liu, C. Li, G. Zhang, L. Yan, Z. Li, Direct synthesis of dimethyl carbonate from CO_2 and methanol over CaO–CeO2 catalysts: the role of acid–base properties and surface oxygen vacancies, New J. Chem. 41 (2017) 12231–12240, https://doi.org/10.1039/C7NJ02606D.

[14] B. Liu, C. Li, G. Zhang, X. Yao, S.S.C. Chuang, Z. Li, Oxygen vacancy promoting dimethyl carbonate synthesis from CO_2 and methanol over Zr-doped CeO2 nanorods, ACS Catal. 8 (2018) 10446–10456.

[15] G. Zhang, Y. Zhou, Y. Yang, T. Kong, Y. Song, S. Zhang, H. Zheng, Elucidating the role of surface Ce4+ and oxygen vacancies of CeO2 in the direct synthesis of dimethyl carbonate from CO_2 and methanol, Molecules 28 (2023) 3785.

[16] D. Salusso, G. Grillo, M. Manzoli, M. Signorile, S. Zafeiratos, M. Barreau, A. Damin, V. Crocellà, G. Cravotto, S. Bordiga, CeO2 frustrated Lewis pairs improving CO_2 and CH3OH conversion to monomethylcarbonate, ACS Appl. Mater. Interfaces 15 (2023) 15396–15408, https://doi.org/10.1021/acsami.2c22122.

[17] L. Chen, S. Wang, J. Zhou, Y. Shen, Y. Zhao, X. Ma, Dimethyl carbonate synthesis from carbon dioxide and methanol over CeO 2 versus over ZrO 2: comparison of mechanisms, RSC Adv. 4 (2014) 30968–30975.

[18] C. Daniel, D. Farrusseng, Y. Schuurman, Investigating the reaction mechanism of dimethyl carbonate synthesis through isotopic labeling experiments, Catal. Commun. (2023) 106697.

[19] K. Tomishige, T. Sakaihori, Y. Ikeda, K. Fujimoto, A novel method of direct synthesis of dimethyl carbonate from methanol and carbon dioxide catalyzed by zirconia, Catal. Lett. 58 (1999) 225–229.

[20] Q. Wang, D. Astruc, State of the art and prospects in metal–organic framework (MOF)-based and MOF-derived nanocatalysis, Chem. Rev. 120 (2019) 1438–1511.

[21] N. Martín, M. Dusselier, D.E. De Vos, F.G. Cirujano, Metal-organic framework derived metal oxide clusters in porous aluminosilicates: a catalyst design for the synthesis of bioactive aza-heterocycles, ACS Catal. 9 (2019) 44–48, https://doi.org/10.1021/acscatal.8b03908.

[22] A. Pustovarenko, A. Dikhtiarenko, A. Bavykina, L. Gevers, A. Ramírez, A. Russkikh, S. Telalovic, A. Aguilar, J.-L. Hazemann, S. Ould-Chikh, J. Gascon, Metal–organic framework-derived synthesis of cobalt indium catalysts for the hydrogenation of CO_2 to methanol, ACS Catal. 10 (2020) 5064–5076, https://doi.org/10.1021/acscatal.0c00449.

[23] X. Lu, X. Li, F. Chen, C. Ni, Z. Chen, Hydrothermal synthesis of prism-like mesocrystal CeO2, J. Alloy. Compd. 476 (2009) 958–962.

[24] T. Yu, J. Joo, Y.Il Park, T. Hyeon, Large-scale nonhydrolytic sol–gel synthesis of uniform-sized ceria nanocrystals with spherical, wire, and tadpole shapes, Angew. Chem. Int. Ed. 44 (2005) 7411–7414, https://doi.org/10.1002/anie.200500992.

[25] A.S. Deshpande, N. Pinna, P. Beato, M. Antonietti, M. Niederberger, Synthesis and characterization of stable and crystalline Ce1-xZrxO2 nanoparticle sols, Chem. Mater. 16 (2004) 2599–2604, https://doi.org/10.1021/cm040155w.

[26] X. Liu, L. Zhang, J. Wang, Design strategies for MOF-derived porous functional materials: preserving surfaces and nurturing pores, J. Mater. 7 (2021) 440–459.

[27] Y. Jiang, J. Gao, Q. Zhao, Z. Liu, M. Fu, J. Wu, Y. Hu, D. Ye, Enhanced oxygen vacancies to improve ethyl acetate oxidation over MnOx-CeO2 catalyst derived from MOF template, Chem. Eng. J. 371 (2019) 78–87.

[28] J. Mei, Y. Shen, Q. Wang, Y. Shen, W. Li, J. Zhao, J. Chen, S. Zhang, Roles of oxygen species in low-temperature catalytic o-xylene oxidation on MOF-derived bouquetlike CeO2, ACS Appl. Mater. Interfaces 14 (2022) 35694–35703.

[29] X. Chen, X. Chen, E. Yu, S. Cai, H. Jia, J. Chen, P. Liang, In situ pyrolysis of Ce-MOF to prepare CeO2 catalyst with obviously improved catalytic performance for toluene combustion, Chem. Eng. J. 344 (2018) 469–479, https://doi.org/10.1016/j.cej.2018.03.091.

[30] J. Mei, S. Zhang, G. Pan, Z. Cheng, J. Chen, J. Zhao, Surfactant-assisted synthesis of MOF-derived CeO2 for low-temperature catalytic catalytic o-xylene combustion, J. Environ. Chem. Eng. 10 (2022) 108743, https://doi.org/10.1016/j.jece.2022.108743.

[31] P.C. Nagajiyothi, R. Ramaraghavulu, K. Pavani, J. Shim, Catalytic reduction of methylene blue and rhodamine B using Ce-MOF-derived CeO2 catalyst, Mater. Lett. (2023) 133837.

[32] W. Sun, X. Li, C. Sun, Z. Huang, H. Xu, W. Shen, Insights into the pyrolysis processes of Ce-MOFs for preparing highly active catalysts of toluene combustion, Catalysts 9 (2019) 682.

[33] G. Chen, M. Mao, L. Chen, G. Zhang, Z. Wang, F. Liu, D. Ye, J. Wu, Enhanced plasma-catalytic oxidation of methanol over MOF-derived CeO2 catalysts with exposed active sites, J. Environ. Chem. Eng. 10 (2022) 108981.

[34] D. Salusso, S. Mauri, G. Deplano, P. Torelli, S. Bordiga, S. Rojas-Buzo, MOF-derived CeO2 and CeZrOx solid solutions: exploring Ce reduction through FTIR and NEXAFS spectroscopy, Nanomaterials 13 (2023) 272.

[35] W. Li, K. Wang, J. Huang, X. Liu, D. Fu, J. Huang, Q. Li, G. Zhan, MxOy–ZrO2 (M = Zn, Co, Cu) solid solutions derived from schiff base-bridged UiO-66 composites as high-performance catalysts for CO_2 hydrogenation, ACS Appl. Mater. Interfaces 11 (2019) 33263–33272, https://doi.org/10.1021/acsami.9b11547.

[36] D. Sun, L. Ye, F. Sun, H. García, Z. Li, From mixed-metal MOFs to carbon-coated Core–Shell metal alloy@ metal oxide solid solutions: transformation of Co/Ni-MOF-74 to Co x Ni1–x@ Co y Ni1–y O@ C for the oxygen evolution reaction, Inorg. Chem. 56 (2017) 5203–5209.

[37] K.-M. Leung, C.-K.J. Tsui, C.-K. Ho, C.-Z. Liao, H.-T. Yau, K.-Y. Chan, C.-Y.V. Li, UiO66-derived catalyst for low temperature catalytic reduction of NO with NH3, ACS Omega 8 (2023) 12362–12371.

[38] K.A. Lomachenko, J. Jacobsen, A.L. Bugaev, C. Atzori, F. Bonino, S. Bordiga, N. Stock, C. Lamberti, Exact stoichiometry of Ce x Zr6–x cornerstones in mixed-metal UiO-66 metal–organic frameworks revealed by extended X-ray absorption fine structure spectroscopy, J. Am. Chem. Soc. 140 (2018) 17379–17383.

[39] M. Signorile, D. Salusso, V. Crocellà, M.C. Paganini, S. Bordiga, F. Bonino, D. Ferri, Surface species in direct liquid phase synthesis of dimethyl carbonate from methanol and CO_2: an MCR-ALS augmented ATR-IR study, Phys. Chem. Chem. Phys. 25 (2023) 8392–8402, https://doi.org/10.1039/D2CP05800F.

[40] M. Lammert, M.T. Wharmby, S. Smolders, B. Bueken, A. Lieb, K.A. Lomachenko, D. De Vos, N. Stock, Cerium-based metal organic frameworks with UiO-66 architecture: synthesis, properties and redox catalytic activity, Chem. Commun. 51 (2015) 12578–12581, https://doi.org/10.1039/C5CC02606G.

[41] M. Lammert, C. Glißmann, N. Stock, Tuning the stability of bimetallic Ce(iv)/Zr (iv)-based MOFs with UiO-66 and MOF-808 structures, Dalton Trans. 46 (2017) 2425–2429, https://doi.org/10.1039/C7DT00259A.

[42] C. Gionco, M.C. Paganini, E. Giamello, O. Sacco, V. Vaiano, D. Sannino, Rare earth oxides in zirconium dioxide: how to turn a wide band gap metal oxide into a visible light active photocatalyst, J. Energy Chem. 26 (2017) 270–276, https://doi.org/10.1016/j.jechem.2016.07.006.

[43] S. Hernández, C. Gionco, T. Husak, M. Castellino, J.A. Muñoz-Tabares, K.R. Tolod, E. Giamello, M.C. Paganini, N. Russo, Insights into the sunlight-driven water oxidation by Ce and Er-doped ZrO 2, Front Chem. 6 (2018) 368.

[44] J. Rodríguez-Carvajal, Recent developments of the program FULLPROF, commission on powder diffraction, IUCr Newsl., 26 (2001) 12–19.

[45] P. Thompson, D.E. Cox, J.B. Hastings, Rietveld refinement of Debye–Scherrer synchrotron X-ray data from Al2O3, J. Appl. Crystallogr 20 (1987) 79–83.

[46] J. Jaumot, R. Gargallo, A. de Juan, R. Tauler, A graphical user-friendly interface for MCR-ALS: a new tool for multivariate curve resolution in MATLAB, Chemom. Intell. Lab. Syst. 76 (2005) 101–110, https://doi.org/10.1016/j.chemolab.2004.12.007.

[47] C. Castán-Guerrero, D. Krizmancic, V. Bonanni, R. Edla, A. Deluisa, F. Salvador, G. Rossi, G. Panaccione, P. Torelli, A reaction cell for ambient pressure soft x-ray absorption spectroscopy, Rev. Sci. Instrum. 89 (2018) 054101, https://doi.org/10.1063/1.5019333.

[48] D.H. Simonne, A. Martini, M. Signorile, A. Piovano, L. Braglia, P. Torelli, E. Borfecchia, G. Ricchiardi, THORONDOR: a software for fast treatment and analysis of low-energy XAS data, J. Synchrotron Radiat. 27 (2020) 1741–1752.

[49] C.E. Hori, H. Permana, K.Y.S. Ng, A. Brenner, K. More, K.M. Rahmoeller, D. Belton, Thermal stability of oxygen storage properties in a mixed CeO2-ZrO2 system, Appl. Catal. B 16 (1998) 105–117.

[51] Y. Guo, Q. Yu, H. Fang, H. Wang, J. Han, Q. Ge, X. Zhu, Ce–UiO-66 derived CeO2 octahedron catalysts for efficient ketonization of propionic acid, Ind. Eng. Chem. Res. 59 (2020) 17269–17278.

[52] J. Mei, Y. Shen, Q. Wang, Y. Shen, W. Li, J. Zhao, J. Chen, S. Zhang, Roles of oxygen species in low-temperature catalytic o-xylene oxidation on MOF-derived bouquetlike CeO2, ACS Appl. Mater. Interfaces 14 (2022) 35694–35703, https://doi.org/10.1021/acsami.2c08418.

[53] X. Yang, X. Cheng, J. Ma, Y. Zou, W. Luo, Y. Deng, Large-pore mesoporous CeO2–ZrO2 solid solutions with in-pore confined Pt nanoparticles for enhanced CO oxidation, Small 15 (2019) 1903058, https://doi.org/10.1002/smll.201903058.

[54] G.S. More, R. Srivastava, Efficient activation of CO_2 over Ce-MOF-derived CeO2 for the synthesis of cyclic urea, urethane, and carbamate, Ind. Eng. Chem. Res. 60 (2021) 12492–12504.

[55] J. Mei, Y. Shen, Q. Wang, Y. Shen, W. Li, J. Zhao, J. Chen, S. Zhang, Roles of oxygen species in low-temperature catalytic o-xylene oxidation on MOF-derived bouquetlike CeO2, ACS Appl. Mater. Interfaces 14 (2022) 35694–35703.

[56] K.I. Hadjiivanov, G.N. Vayssilov, Characterization of oxide surfaces and zeolites by carbon monoxide as an IR probe molecule. in: Advances in Catalysis, Academic Press, 2002, pp. 307–511, https://doi.org/10.1016/S0360-0564(02)47008-3.

[57] C. Yang, X. Yu, S. Heißler, A. Nefedov, S. Colussi, J. Llorca, A. Trovarelli, Y. Wang, C. Wöll, Surface faceting and reconstruction of ceria nanoparticles, Angew. Chem. Int. Ed. 56 (2017) 375–379.

[58] H. Idriss, J. Llorca, Low temperature infrared study of carbon monoxide adsorption on rh/ceo2, Catalysts 9 (2019) 598.

[59] F. Bozon-Verduraz, A. Bensalem, IR studies of cerium dioxide: influence of impurities and defects, J. Chem. Soc., Faraday Trans. 90 (1994) 653–657.

[60] C. Binet, M. Daturi, J.-C. Lavalley, IR study of polycrystalline ceria properties in oxidised and reduced states, Catal. Today 50 (1999) 207–225.

[61] S. Rojas-Buzo, P. Concepción, J.L. Olloqui-Sariego, M. Moliner, A. Corma, Metalloenzyme-inspired Ce-MOF catalyst for oxidative halogenation reactions, ACS Appl. Mater. Interfaces 13 (2021) 31021–31030.

[62] M. Daturi, C. Binet, J.-C. Lavalley, A. Galtayries, R. Sporken, Surface investigation on Ce x Zr 1-x O 2 compounds, Phys. Chem. Chem. Phys. 1 (1999) 5717–5724.

[63] P. Hollins, J. Pritchard, Interactions of CO molecules adsorbed on Cu (111), Surf. Sci. 89 (1979) 486–495.

[64] A. Zecchina, D. Scarano, S. Bordiga, G. Ricchiardi, G. Spoto, F. Geobaldo, IR studies of CO and NO adsorbed on well characterized oxide single microcrystals, Catal. Today 27 (1996) 403–435.

[65] C. Morterra, G. Cerrato, S. Di Ciero, IR study of the low temperature adsorption of CO on tetragonal zirconia and sulfated tetragonal zirconia, Appl. Surf. Sci. 126 (1998) 107–128.

[66] C. Schilling, A. Hofmann, C. Hess, M.V. Ganduglia-Pirovano, Raman spectra of polycrystalline CeO2: a density functional theory study, J. Phys. Chem. C 121 (2017) 20834–20849.

[67] O.H. Laguna, F.R. Sarria, M.A. Centeno, J.A. Odriozola, Gold supported on metal-doped ceria catalysts (M= Zr, Zn and Fe) for the preferential oxidation of CO (PROX), J. Catal. 276 (2010) 360–370.

[68] O.H. Laguna, A. Pérez, M.A. Centeno, J.A. Odriozola, Synergy between gold and oxygen vacancies in gold supported on Zr-doped ceria catalysts for the CO oxidation, Appl. Catal. B 176 (2015) 385–395.

[69] A. Trovarelli, Catalytic properties of ceria and CeO2-containing materials, Catal. Rev. 38 (1996) 439–520.

[70] J.A. Munoz Tabares, M.J. Anglada, Quantitative analysis of monoclinic phase in 3Y-TZP by Raman spectroscopy, J. Am. Ceram. Soc. 93 (2010) 1790–1795.

[71] G.B. Della Mea, L.P. Matte, A.S. Thill, F.O. Lobato, E.V. Benvenutti, L.T. Arenas, A. Jürgensen, R. Hergenröder, F. Poletto, F. Bernardi, Tuning the oxygen vacancy population of cerium oxide (CeO2−x, 0<x<0.5) nanoparticles, Appl. Surf. Sci. 422 (2017) 1102–1112, https://doi.org/10.1016/j.apsusc.2017.06.101.

[72] T. Montini, M. Melchionna, M. Monai, P. Fornasiero, Fundamentals and catalytic applications of CeO2-based materials, Chem. Rev. 116 (2016) 5987–6041.

[73] D.R. Mullins, M.D. Robbins, J. Zhou, Adsorption and reaction of methanol on thin-film cerium oxide, Surf. Sci. 600 (2006) 1547–1558, https://doi.org/10.1016/j.susc.2006.02.011.

[74] V. Matolín, J. Libra, M. Škoda, N. Tsud, K.C. Prince, T. Skála, Methanol adsorption on a CeO2(111)/Cu(111) thin film model catalyst, Surf. Sci. 603 (2009) 1087–1092, https://doi.org/10.1016/j.susc.2009.02.010.

[75] Z. Yang, T.K. Woo, K. Hermansson, Effects of Zr doping on stoichiometric and reduced ceria: a first-principles study, J. Chem. Phys. 124 (2006).

[76] L. Li, W. Liu, R. Chen, S. Shang, X. Zhang, H. Wang, H. Zhang, B. Ye, Y. Xie, Atom-economical synthesis of dimethyl carbonate from CO2: engineering reactive frustrated lewis pairs on ceria with vacancy clusters, Angew. Chem. Int. Ed. 61 (2022) e202214490, https://doi.org/10.1002/anie.202214490.

[77] K.T. Jung, A.T. Bell, An in situ infrared study of dimethyl carbonate synthesis from carbon dioxide and methanol over zirconia, J. Catal. 204 (2001) 339–347, https://doi.org/10.1006/jcat.2001.3411.

[78] M.L. Unland, Infrared study of methanol decomposition on alkali metal X-type zeolites, J. Phys. Chem. 82 (1978) 580–583, https://doi.org/10.1021/j100494a016.

[79] W.G. Reimers, M.M. Branda, Methanol decomposition on low index and stepped CeO2 surfaces from GGA+ U, Appl. Surf. Sci. 394 (2017) 509–518.

[80] V. Matolín, J. Libra, M. Škoda, N. Tsud, K.C. Prince, T. Skála, Methanol adsorption on a CeO2 (1 1 1)/Cu (1 1 1) thin film model catalyst, Surf. Sci. 603 (2009) 1087–1092.

[81] J. Kondo, H. Abe, Y. Sakata, K. Maruya, K. Domen, T. Onishi, Infrared studies of adsorbed species of H2, CO and CO2 over ZrO2, J. Chem. Soc., Faraday Trans. 1: Phys. Chem. Condens. Phases 84 (1988) 511–519, https://doi.org/10.1039/F19888400511.

[82] K. Pokrovski, K.T. Jung, A.T. Bell, Investigation of CO and CO2 adsorption on tetragonal and monoclinic zirconia, Langmuir 17 (2001) 4297–4303, https://doi.org/10.1021/la001723z.

[83] E.-M. Köck, M. Kogler, T. Bielz, B. Klötzer, S. Penner, In situ FT-IR spectroscopic study of CO2 and CO adsorption on Y2O3, ZrO2, and Yttria-stabilized ZrO2, J. Phys. Chem. C 117 (2013) 17666–17673, https://doi.org/10.1021/jp405625x.

[84] G. Busca, V. Lorenzelli, Infrared spectroscopic identification of species arising from reactive adsorption of carbon oxides on metal oxide surfaces, Mater. Chem. 7 (1982) 89–126, https://doi.org/10.1016/0390-6035(82)90059-1.

[85] J.C. Lavalley, Infrared spectrometric studies of the surface basicity of metal oxides and zeolites using adsorbed probe molecules, Catal. Today 27 (1996) 377–401, https://doi.org/10.1016/0920-5861(95)00161-1.

[86] G.N. Vayssilov, M. Mihaylov, P.S. Petkov, K.I. Hadjiivanov, K.M. Neyman, Reassignment of the vibrational spectra of carbonates, formates, and related surface species on ceria: a combined density functional and infrared spectroscopy investigation, J. Phys. Chem. C 115 (2011) 23435–23454.

[87] L. Chen, S. Wang, J. Zhou, Y. Shen, Y. Zhao, X. Ma, Dimethyl carbonate synthesis from carbon dioxide and methanol over CeO 2 versus over ZrO 2: comparison of mechanisms, RSC Adv. 4 (2014) 30968–30975.

[88] S.-Y. Zhao, S.-P. Wang, Y.-J. Zhao, X.-B. Ma, An in situ infrared study of dimethyl carbonate synthesis from carbon dioxide and methanol over well-shaped CeO2, Chin. Chem. Lett. 28 (2017) 65–69.

[89] C. Copéret, D.P. Estes, K. Larmier, K. Searles, Isolated surface hydrides: formation, structure, and reactivity, Chem. Rev. 116 (2016) 8463–8505, https://doi.org/10.1021/acs.chemrev.6b00082.

[90] Z. Wu, Y. Cheng, F. Tao, L. Daemen, G.S. Foo, L. Nguyen, X. Zhang, A. Beste, A. J. Ramirez-Cuesta, Direct neutron spectroscopy observation of cerium hydride species on a cerium oxide catalyst, J. Am. Chem. Soc. 139 (2017) 9721–9727, https://doi.org/10.1021/jacs.7b05492.

[91] Z.-F. Zhang, Z.-T. Liu, Z.-W. Liu, J. Lu, DMC formation over Ce0.5Zr0.5O2 prepared by complex-decomposition method, Catal. Lett. 129 (2009) 428–436, https://doi.org/10.1007/s10562-008-9816-7.

[92] Z.-F. Zhang, Z.-W. Liu, J. Lu, Z.-T. Liu, Synthesis of dimethyl carbonate from carbon dioxide and methanol over CexZr1-xO2 and [EMIM]Br/Ce0.5Zr0.5O2, Ind. Eng. Chem. Res. 50 (2011) 1981–1988, https://doi.org/10.1021/ie102017j.

[93] P. Kumar, P. With, V.C. Srivastava, R. Shukla, R. Gläser, I.M. Mishra, Dimethyl carbonate synthesis from carbon dioxide using ceria–zirconia catalysts prepared using a templating method: characterization, parametric optimization and chemical equilibrium modeling, RSC Adv. 6 (2016) 110235–110246, https://doi.org/10.1039/C6RA22643D.

[94] J. Al-Darwish, M. Senter, S. Lawson, F. Rezaei, A.A. Rownaghi, Ceria nanostructured catalysts for conversion of methanol and carbon dioxide to dimethyl carbonate, Catal. Today 350 (2020) 120–126, https://doi.org/10.1016/j.cattod.2019.06.013.

[95] K. Tomishige, K. Kunimori, Catalytic and direct synthesis of dimethyl carbonate starting from carbon dioxide using CeO2-ZrO2 solid solution heterogeneous catalyst: effect of H2O removal from the reaction system, Appl. Catal. A Gen. 237 (2002) 103–109.

[96] S. Xu, Y. Cao, Z. Liu, Dimethyl carbonate synthesis from CO2 and methanol over CeO2-ZrO2 catalyst, Catal. Commun. 162 (2022) 106397.